applied sciences

MDPI

*Article*

# Optimization of Aquifer Monitoring through Time-Lapse Electrical Resistivity Tomography Integrated with Machine-Learning and Predictive Algorithms

**Valeria Giampaolo [1,*], Paolo Dell'Aversana [2], Luigi Capozzoli [1], Gregory De Martino [1] and Enzo Rizzo [3]**

[1] National Research Council, Institute of Methodologies for Environmental Analysis, CNR-IMAA, 85052 Tito, Italy
[2] Eni SpA, San Donato Milanese, Milan 20097, Italy
[3] Department of Physics and Earth Sciences, University of Ferrara, 44121 Ferrara, Italy
* Correspondence: valeria.giampaolo@imaa.cnr.it

**Featured Application: In this work, Vector Autoregressive and Recurrent Neural Network algorithms are used to predict time-space evolution of a saline water plume in homogeneous and real aquifers.**

**Abstract:** In this paper, an integrated workflow aimed at optimizing aquifer monitoring and management through time-lapse Electric Resistivity Tomography (TL-ERT) combined with a suite of predictive algorithms is discussed. First, the theoretical background of this approach is described. Then, the proposed approach is applied to real geoelectric datasets recorded through experiments at different spatial and temporal scales. These include a sequence of cross-hole resistivity surveys aimed at monitoring a tracer diffusion in a real aquifer as well as in a laboratory experimental set. Multiple predictive methods were applied to both datasets, including Vector Autoregressive (VAR) and Recurrent Neural Network (RNN) algorithms, over the entire sequence of ERT monitor surveys. In both field and lab experiments, the goal was to retrieve a determined number of "predicted" pseudo sections of apparent resistivity values. By inverting both real and predicted datasets, it is possible to define a dynamic model of time-space evolution of the water plume contaminated by a tracer injected into the aquifer system(s). This approach allowed for describing the complex fluid displacement over time conditioned by the hydraulic properties of the aquifer itself.

**Keywords:** multi temporal geophysics; cross-hole geoelectrical measurements; Vector Autoregressive algorithms; Recurrent Neural Networks; aquifer monitoring



**Citation:** Giampaolo, V.; Dell'Aversana, P.; Capozzoli, L.; De Martino, G.; Rizzo, E. Optimization of Aquifer Monitoring through Time-Lapse Electrical Resistivity Tomography Integrated with Machine-Learning and Predictive Algorithms. *Appl. Sci.* **2022**, *12*, 9121. https://doi.org/10.3390/app12189121

Academic Editor: Dario De Domenico

Received: 5 August 2022
Accepted: 5 September 2022
Published: 11 September 2022



## 1. Introduction

In the recent centuries, climate change-related phenomena and the rapid increase in population have dramatically increased the exploitation of freshwater resources causing deterioration in groundwater quality and raising the probability of severe droughts. Therefore, the demand for better information on groundwater quantity and quality trends and how best to equitably manage them is growing worldwide [1–3]. However, these trends consist of an integrated response to several climatic, anthropogenic, and hydrogeological factors and their interactions, which makes prediction both for the short and long term a challenging task.

Natural geological systems exhibit a large spatial variability of hydrogeological properties over a wide range of scales. Numerical modelling is often performed to gain an understanding of the hydraulic nature of the aquifer and to predict contaminant transport; these models require spatial distributions of hydraulic properties as inputs [4]. It is typically not feasible to describe the hydraulic properties over the entire flow domain at the resolution needed for accurate flow modelling using conventional hydraulic property

measurement techniques alone [5,6]. The ability to describe adequately these properties is strongly dependent on the availability and distribution of field measurements correlated with the hydrological heterogeneities [7].

The need for a comprehensive understanding of fluid transport behavior, such as flow pathways, flow velocity, and hydraulic conductivity in heterogeneous aquifers, has driven improvements of near-surface geophysical methods able to provide densely spatial and temporal knowledge about these subsurface properties [8–11]. Among others, the direct current (DC) method is probably the most widely used near-surface geophysical techniques for these scopes because subsurface electrical resistivity properties are correlated to physical, chemical, and lithologic properties of subsoil (e.g., saturation and salinity of fluids within the pore space, porosity, and clay content). Furthermore, measurement techniques are highly scalable, allowing for investigations at depths to tens of centimeters to hundreds of meters [12,13].

In the last two decades, the DC electrical resistivity method has evolved significantly through the introduction of cross-hole electrical resistivity tomography (CH-ERT) [14] and 3D or 4D monitoring by time-lapse surveys as well as permanent measurement systems [15–19]. Nowadays, CH-ERT, combined with time-lapse surveys, has become very common in environmental investigations to quantify the hydraulic parameters and to obtain information on the spatial variability of solute transport processes allowing for better deep resolution and anisotropy detection compared to surface measurements [20,21].

This type of survey commonly produces large volumes of data in the form of time series, representing how resistivity distribution changes in the subsoil over time. These variations can be correlated to various possible causes, such as water injection/production, pollution diffusion, and so forth [22–24].

If a sufficiently large historical database is available, it is possible to make probabilistic predictions about future resistivity changes by applying statistical and predictive algorithms to time-lapse ERT data. So, the total knowledge acquired about past, current, and predicted fluid displacement, contaminant diffusion, and aquifer hydraulic properties can be used to define an optimal policy of aquifer management.

In general, the main objective of time series analysis is to extract meaningful characteristics and statistical information from data organized in chronological order for different purposes, such as analysis of past behavior, prediction, and forecasting of future trends, curve fitting, interpolation and extrapolation, classification and clustering, segmentation and decomposition, frequency characterization, etc. [25]. There are numerous types of data analysis approaches available for time series that are suitable for understanding and forecasting patterns of one or more crucial variables that characterize dynamic systems. Among the others, univariate and multivariate analysis approaches and Deep Neural Networks have proven to be very useful for the scope [4,7,26,27]. The various methods show different effectiveness depending on their application to univariate or multivariate time series. A univariate time series is a data series with a single time-dependent variable. On the contrary, in multivariate time series each variable depends both on its past values and, to some extent, also on other variables. That dependency can be used for improving the forecasting of future values and trends [28].

In detail, the Recurrent Neural Networks (RNN), like the other artificial neural networks, utilize training data to learn, with the final objective to find the "optimal" weight matrixes that allow for minimizing the misfit between the actual and predicted output. However, RNN's distinctive characteristic consists in their "memory" capability: this consists of their ability to take information from prior inputs to influence both current input and output. In fact, in traditional neural networks, all inputs are assumed independent from the outputs; instead, in RNNs, it is assumed that there is some significant correlation between input and output. In detail, the RNNs structure includes a "time delay unit" and a "feedback connection" to use information from a previous state for inferring a model in the subsequent state. This allows for a wide range of applications to the predictive analysis of many types of time series, including natural language analysis, image captioning,

speech and handwriting recognition, text summarization, text generation, word prediction, stock market prediction, call center data analysis, sentiment analysis, face detection, image recognition, and so forth [29]. For instance, RNN's outperform traditional models in some hydrogeological applications, such as groundwater level and quality prediction [30,31].

In general, statistical and artificial neural networks have been successful applied to data series in near surface geophysics over multiple monitor surveys [32–34] and have produced consistent results when applied to time-lapse resistivity survey addressed to optimizing oil production and $CO_2$ geological storage and predicting the future behavior of soils in slopes [35–37]. However, only one example of RNN application to near surface geophysical data forecasting is reported in literature by Alali et al. [38], who used RNN to produce synthetic time-lapse seismic data.

In this study, statistical and deep learning algorithms were tested to predict saline plume migration in two porous aquifers using cross-hole geoelectrical datasets recorded through experiments at different spatial and temporal scales (a real aquifer and a laboratory experimental set-up). In detail, the Vector Auto Regressive (VAR) method and Recurrent Neural Networks (RNN) were selected. As the other types of time series, the multi temporal CH-ERT datasets acquired in the field and laboratory experiments produced a large volume of data that are very suitable for statistical-based approaches and RNN's application. Because of resistivity changes over time in the subsoil due to a fluid movement, high spatial correlation between electrical resistivity measurements taken along the same layout can be reasonably expected. For this reason, these time-lapse datasets represent a multivariate time series.

The following sections describe how to apply both VAR and RNN methods with the final goal to retrieve a multivariate forecast model of the aquifers and of fluids displacements over time.

## 2. Background Theory

This section briefly describes the basic principles of DC electrical method and the fundamentals of the two categories of predictive methods used: statistical-based approaches and Recurrent Neural Networks.

### 2.1. DC Electrical Method

As shown in Figure 1, the DC electrical method consists in injecting a current ($I_{AB}$, Ampere) into the subsoil by using two current electrodes $A$ and $B$ and to measure the potential difference ($\Delta V_{MN}$, Volt) through two other electrodes $M$ and $N$ on the ground surface. The resistance of the material ($R$, $\Omega$) through which the current flows can be obtained by:

$$\Delta V_{MN} = I_{AB} R. \quad (1)$$

$R$ depends on electrical resistivity distribution of the subsoil ($\rho_a$, $\Omega$m) and the configuration of electrodes, according to:

$$\rho_a = K_g R \quad (2)$$

where $K_g$ (m) is called geometric factor; it depends on electrodes geometry (array) and can be calculated by:

$$K_g = 2\pi \left[ \left( \frac{1}{AM} - \frac{1}{BM} - \frac{1}{AN} + \frac{1}{BN} \right) \right]^{-1}. \quad (3)$$

For inhomogeneous and anisotropic media, $\rho_a$ is called apparent resistivity and is defined as the ratio between the measured value of the parameter in question and its theoretical value in a homogeneous and isotropic medium of unit resistivity [39]. Therefore, in real cases, inverse methods must be applied to turn from the apparent resistivity to the true spatial distribution of this parameter.

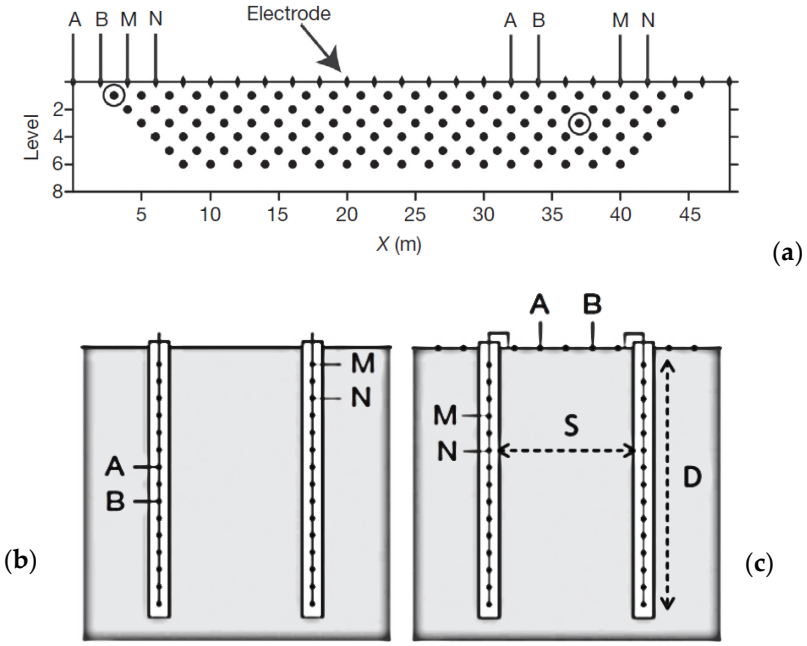


**Figure 1.** (**a**) Pseudo section setting for ERT acquisition with Dipole Dipole (DD) array, (**b**) cross borehole, and (**c**) cross borehole with surface. *A*, *B*, *M*, and *N* are electrodes. D is borehole depth; S is borehole separation. D/S > 1.5. Adapted from [14].

Lateral and vertical resistivity variation of the subsoil can be determined by moving current (*AB*) and receiving dipoles (*MN*) on the soil surface. This is called electrical resistivity tomography (ERT) and the sequence of four electrodes *A*, *B*, *M* and *N* is defined as quadrupoles.

In order to increase resolution at depth, Shima [40] and Zhou and Greenhalgh [41] introduced the cross-hole electrical resistivity tomography (CH-ERT). In this case, plate or cylindrical electrodes are installed along two or more boreholes in contact with the host soils/rocks or with the formation fluid (Figure 1b). CH-ERT allows to identify lateral and vertical resistivity variations in the area between two or more boreholes; however, the ratio between boreholes depth and separation should be >1.5 otherwise sensitivity is reduced (Figure 1c).

### *2.2. Predictive Methods*

#### 2.2.1. Statistical Approaches

A relatively simple statistical approach for time series analysis is known as Exponential Smoothing. This is based on a weighted sum of past observations and applies an exponentially decreasing weight for past observations [42]. Several variants of this approach exist. The simplest one is called Single Exponential Smoothing (SES, for short). This is effective for univariate data that do not show neither significant trends nor seasonality. A more complex approach is the Double Exponential Smoothing method that includes the information about trends in the data. Triple Exponential Smoothing is a further extension of the previous approaches. It considers the seasonality eventually presents in the time series.

In case datasets are characterized by variables that show a significant reciprocal correlation, methods based on multivariate analysis (MVA) are used [43–45]. This correlation can be exploited for forecasting future values of one or more variables. Such a mutual dependency is often a crucial feature of multiple geophysical measurements used for characterizing dynamic geological models.

Between the various approaches for multivariate time series forecasting, it is possible to applied Vector Auto Regression (VAR) method where each variable is considered a linear function of the past values of itself and the past values of all the other variables [46].

Considering the simplest case in which there are only two correlated variables, $y_1$ and $y_2$, it is possible to forecast the values of these two variables at the future time $t$, using the data recorded for past n values. Furthermore, assuming the correlation between the two variables, the past value of both $y_1$ and $y_2$ will be used.

Formally, in case just one set of past measurements (n = 1) is available, the following relationships can be written:

$$y_{1,t} = c_1 + \phi_{11,1}\, y_{1,t-1} + \phi_{12,1}\, y_{2,t-1} + e_{1,t} \quad (4)$$

$$y_{2,t} = c_2 + \phi_{21,1}\, y_{1,t-1} + \phi_{22,1}\, y_{2,t-1} + e_{2,t}, \quad (5)$$

where $e_{1,t}$ and $e_{2,t}$ are white noise processes that may be contemporaneously correlated. The symbols $c_1$ and $c_2$ are constants serving as the intercepts of the model.

The coefficient $\phi_{ii,\ell}$ represents the influence of the $\ell_{th}$ lag of variable $y_i$ on itself. Instead, the coefficient $\phi_{ij,\ell}$ represents the influence of the $\ell_{th}$ lag of variable $y_j$ on $y_i$, where "lag" represents a fixed amount of passing time [47].

Equations (4) and (5) just state that each individual variable is using the past values of every variable to make the predictions, based on the assumption of significant correlation between these variables. This approach is useful for describing the dynamic behavior of the data and allows for improving the forecast model.

#### 2.2.2. Recurrent Neural Networks

A different approach for time series forecasting is through Recurrent Neural Network (RNN). It represents a class of artificial neural networks characterized by the connection between the nodes along a temporal sequence. This allows for exhibiting temporal dynamic behavior. In detail, RNN's can use an "internal memory state" to process variable-length sequences of inputs in order to predict probabilistic future trends in the data [48].

The simplest RNN consists of just three layers: one input layer with $d$ input neurons, one hidden layer with $c$ hidden neurons, and one output layer with $q$ output neurons (see Figure 2). At each time point $t$, the network includes three matrices of weight, $W_{ih}$, $W_{hh}$, and $W_{ho}$ that connect, the input to hidden layer, recurrent hidden layer to hidden layer itself, and hidden layer to output, respectively. The hidden layer captures information about what happened in the previous time step. It can be considered as the "memory" of the network.

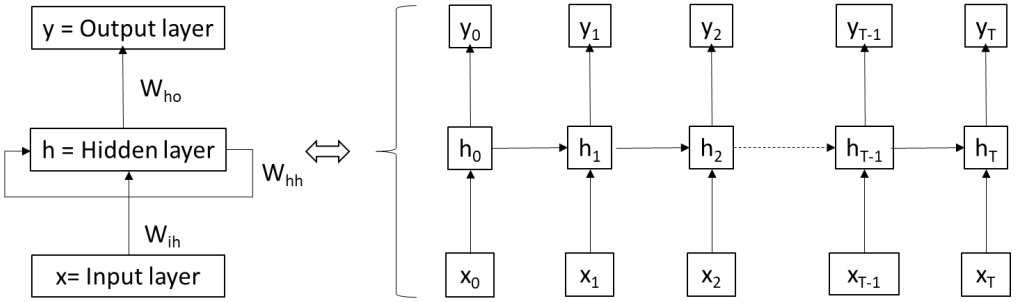


**Figure 2.** Schematic and simplified structure of an RNN.

In order to determine how well the RNN predicts the output during the training phase, a Loss function ($L_t$) is computed that includes the differences between predicted and actual output ($y_t$ and $y'_t$, respectively) at each iteration. At each time step, $L_t$ is given by cross-entropy, defined as follows:

$$L_t = -y_t \log\left(y'_t\right) \quad (6)$$

The final Loss is the sum of the loss at all steps. For instance, in case of $T$ steps (and $T$ layers, as in Figure 2), the final Loss is:

$$L = \sum_{j=1}^{T} L_j \quad (7)$$

The Loss function is minimized by finding the optimal weights for all the nodes forming out the RNN. For instance, the gradient descent algorithm can be applied for determining the optimal weights matrixes. According with that algorithm, the rule for updating the weights is:

$$W = W - \alpha \frac{\partial L}{\partial W} \quad (8)$$

Here, $W$ indicates, generically, each one of the weights matrixes defined above ($W_{ih}$, $W_{hh}$ and $W_{ho}$). The parameter $\alpha$ is called "learning rate". It scales the gradient and thus controls the step size. When the gradient of the Loss function is calculated with respect to the weight matrixes, generally it is possible to incur in the well-known problem of the vanishing gradient. In fact, when the RNN is formed by many neural layers, there is the risk that the gradient tends to become smaller and smaller at each derivative step. Consequently, since the gradient tends to vanish over time, the network cannot learn properly about long-term time information kept in memory. This is a typical problem in all the types of deep neural networks formed by many hidden layers, and not exclusively in RNNs. In order to face that problem, a variant of RNN called "Long-Short Term Memory" (LSTM) algorithm can be used [49–51]. This allows for the network to include both short-term and long-term dependencies at a given time from many time steps before the current time and can solve the vanishing gradient problem effectively. A typical LSTM cell consists of three special "gates" called, respectively, the input gate, forget gate, and output gate. These allow for deciding what information must be included or excluded from the network memory and used for calculating the output. In other words, the effectiveness of the network is guaranteed by selecting the length of the sequence of historical data to be used as "memory information". The LSTM network is designed to keep information in the memory only if required. The input gate is responsible for selecting the part of information that must be stored in memory and used for calculating the output. Instead, the forget gate is responsible for deciding what information is not relevant for calculating the output and should be excluded from the output computation. Finally, the output gate is set for selecting what information must be shown at each time step. It determines the value of the next hidden state that contains information on previous inputs, that is, the output gate determines what output (next Hidden State) to generate from the current Internal Cell State [52–54].

## 3. Datasets

For the present study, time series of subsoil electrical resistivity data (Ωm) variations have been obtained from geophysical monitoring experiments in a test site and in laboratory. The data coming from the test site were already published in a previous experiment obtained through a collaboration between the Department of Environmental Engineering of the University of Calabria and CNR-IMAA [55–58]. Anyway, all the data were re-elaborated with a new inversion approach described below.

In both cases, electrical resistivity variations are due to the introduction, into the studied aquifers, of electrically conductive fluids (saline solutions at the concentration of 100 g/L) in order to enhance resistivity contrasts. The full description of the experimental set-up and the procedure to obtain subsoil resistivity data is provided in the following sections.

### 3.1. Real Scale Field Dataset

The field dataset was acquired to better characterize the groundwater system of the Montalto Uffugo test site [55,59–61]. From a hydrogeological point of view, the test site can be divided in four formations (Figure 3a): a shallow phreatic aquifer (formation A) to a

depth of 7 m; a shale layer from 7 to 11 m (formation B); the main confined aquifer, from 11 to 55 m, which is composed by silty sands alternated to conglomerate and clay lenses (formation C); and the shale substratum (formation D).

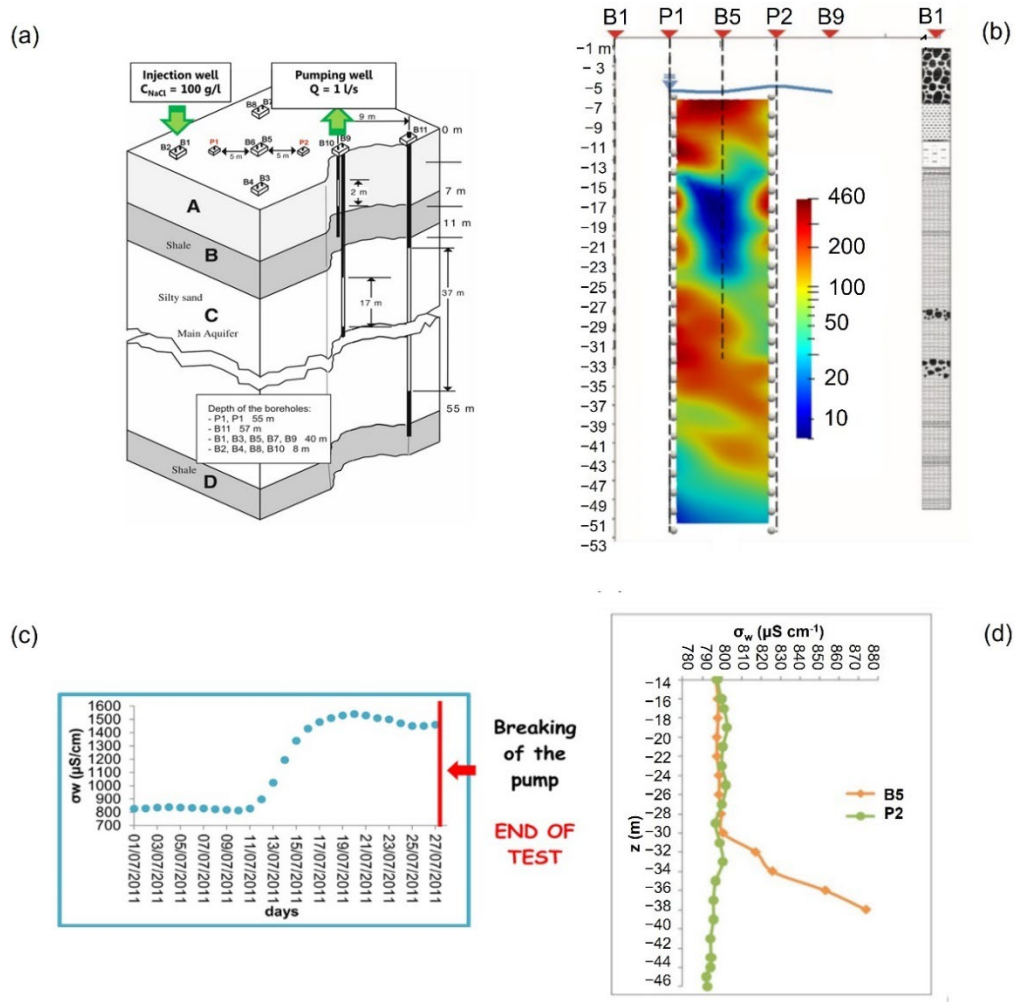


**Figure 3.** (**a**) Tracer test at Montalto Uffugo test site: (Formation A) shallow aquifer; (Formation B) shale; (Formation C) main aquifer, silty sands alternated to conglomerate and clay lenses; (Formation D) shale. B1–11 are boreholes. P1–2 are piezometers for CH-ERT. (**b**) Pre-tracer test resistivity model and B11 stratigraphic log (from 41, modified); (**c**) water electrical conductivity (normalized at 20 °C) monitored in P1 at the depth of 40 m; (**d**) water electrical conductivity (normalized at 20 °C) logs measured 20 days after the salt injection (19 July), in boreholes B5 and P2. Adapted from [55].

The Montalto Uffugo system is monitored by 11 boreholes (B1–11), and two new PVC piezometers (P1 and P2 in Figure 3) were instrumented for CH-ERT measurements. For the confined aquifer, the water table is approximately at −6 m and hydraulic conductivity is in the order of $10^{-5}$ $ms^{-1}$ [55].

A tracer test experiment was carried out at the site by the injection of 400 L of saltwater solution (concentration C = 100 g/L of NaCl) into the confined aquifer C through the borehole B1 (Figure 3). At the same time, to create a water flux longitudinal compared to piezometers P1–P2, 1 L/s of water was pumped in B9. The entire test lasted about 27 days and was stopped before the salt tracer could reach P2, due to the rupture of the pump. The tracer test was monitored by temperature and electrical conductivity of water in the piezometer P1, B5, and P2. In addition, CH-ERT monitoring based on time-lapse geoelectrical survey was carried out [56–58].

A number of 48 steel circular electrodes installed along P1 and P2 were used to perform the CH-ERT measurements within 6–52 m in depth. A total of 87 CH-ERTs (3 at days)

with 1836 measurements for each CH-ERT were taken with reciprocal configuration for errors assessment. Electrical resistivity data were acquired using a dipole–dipole array with injection current dipole and receiver dipole located in different boreholes [56–58].

Figure 3b shows the starting resistivity model acquired two days before the tracer test and inverted using ResIPy software [62,63]. The area under investigation was parameterized using a node-centered, 2D, quadrilateral mesh made by 30 × 66 square elements, covering a region of 128 m × 221 m to account for current flow towards infinite boundaries.

### *3.2. Small-Scale Laboratory Dataset*

The laboratory dataset was acquired during a controlled experiment at Hydrogeosite Laboratory of CNR-IMAA. The aim was to image salt plume migration under almost natural gradient conditions by means of cross-hole electrical resistivity monitoring for quantifying hydraulic conductivity and transport parameters of a homogeneous porous aquifer [64,65].

The simulated phreatic aquifer consists of 1 $m^3$ of homogeneous silica sand (95% $SiO_2$) characterized by an average diameter equal to 0.09 mm (very fine sand), porosity of about 45–50%, and hydraulic conductivity in the order of $10^{-5}$ $ms^{-1}$ [66]. An external hydraulic system was used to impose a constant hydraulic gradient during all the experiment while contamination occurs by continuously injecting 10 liters of salt water (NaCl solution with a concentration of 100 g/L) for 10 days. The source of contamination was at −0.15 m of depth (Figure 4).

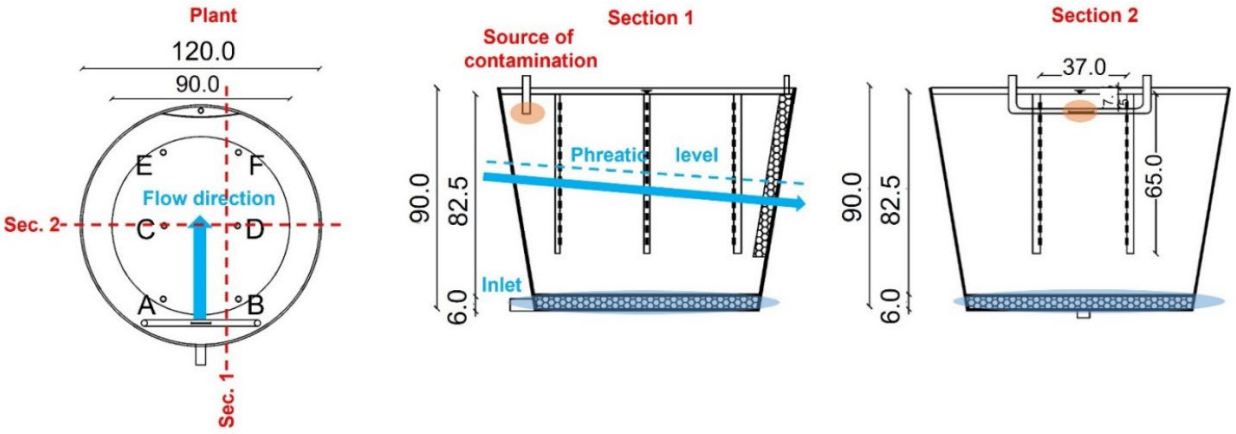


**Figure 4.** Laboratory experimental set-up. A–F are the piezometers instrumented for CH-ERT. Distances are in cm. Modified from [65].

The geophysical system used to monitor the plume migration consisted of six piezometers (A–F in Figure 4) instrumented for CH-ERT as shown in Figure 4. In detail, 12 steel electrodes (plate of 0.5 cm) were installed along the six piezometers and used to perform the 2D cross-borehole resistivity measures within −0.1−−0.65 m in depth. In addition, pH, Eh, temperature, and electrical conductivity of water were monitored for 31 days both in the piezometer A and at the outlet [64,65].

The entire geophysical dataset consists of 210 CH-ERTs with 504 measurements with reciprocal for errors assessment. Recurrent Neural Networks (RNN) were applied to time-lapse geoelectrical measurements for predicting the displacement of the contaminant over time in the small-scale laboratory experimental setup. In this work only measurements between piezometers C and D (transversal section respect to the plume migration) were considered. In detail, the first 15 daily surveys as the historical dataset (7560 data) were used for training the recurrent network. Then, the data belonging to the remaining five sets of measurements (2520 data) were used as "test data" for checking the predictive capabilities of implemented RNN. Figure 5 shows a subset of data (in terms of apparent resistivity) taken at several measurement points.

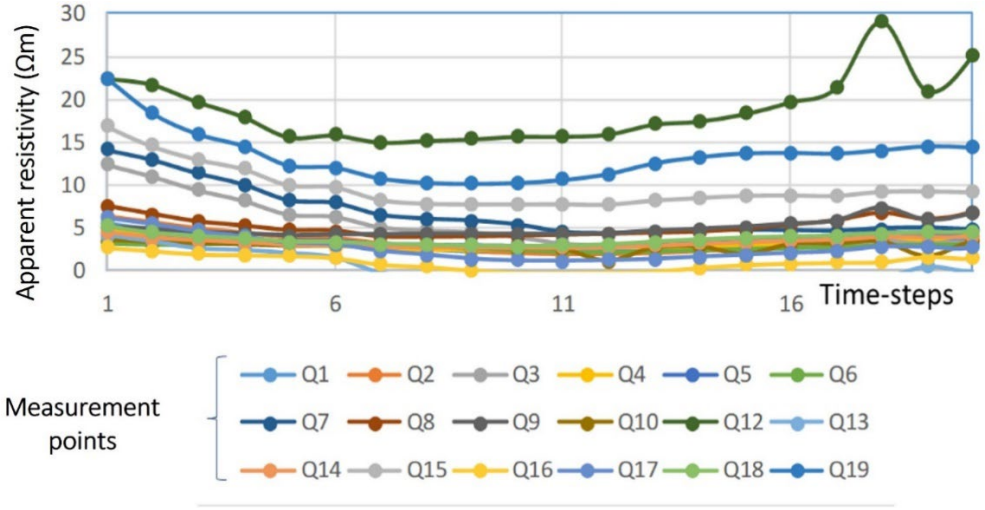


**Figure 5.** Subset of data (in terms of apparent resistivity) taken at several measurement points, in the set-up of Figure 4, over 20 time steps. Q is quadrupole.

## 4. Results

In this study, Vector Autoregressive (VAR) and Recurrent Neural Network were applied to TL-ERT measurements for the forecast of the displacement of a salt tracer and a contaminant plume over time in porous aquifers. As described in Section 3, two datasets were considered for the performance analysis of the aforementioned forecasting algorithms: a small-scale laboratory and a real scale field experimental setup.

For our computations and tests, we used a proprietary workflow based on Python libraries including Tensorflow. Among the many libraries available in the public domain, we used Keras, which represents an effective package for applying Recurrent Neural Networks to many types of time series. Keras is a deep learning Application Programming Interface (API) written in Python (version 3), running on top of the machine-learning platform TensorFlow mentioned above. For data analysis and result plotting, we used libraries fully available in the public domain like Pandas, Numpy, and Matplotlib.

Table 1 gives a summary of the apparent electrical resistivity dataset considered for analysis in the present manuscript.

**Table 1.** Description of the two datasets used in the present manuscript for testing Vector Autoregressive (VAR) and Recurrent Neural Network algorithms (RNN).

| Electrical Resistivity Dataset | Number of Surveys in Training Data | Number of Surveys in Test Data |
|---|---|---|
| Field data | 2–20 CH-ERT (1836 data each) | 5 CH-ERT (1836 data each) |
| Laboratory data | 2–20 CH-ERT (504 data each) | 5 CH-ERT (504 data each) |

Cross-hole electrical resistivity tomography (CH-ERT).

### *4.1. Application of VAR and RNN Methods to Field Dataset*

This first example shows the predictive results when the Vector Autoregressive (VAR) and Recurrent Neural Network (RNN) methods are applied to multi temporal CH-ERT field dataset described in Section 3.1. The objective was to predict the displacement of the saline tracer if the pump had not broken.

As described in Section 2.2.1, VAR is a statistical multivariate forecasting algorithm that is used when two or more time series influence each other. Typical examples of multivariate time series are time-lapse electric resistivity measurements. These are used for retrieving models of the resistivity distribution that change over time for some geological reason.

To retrieve a defined number of "predicted" pseudo sections of apparent resistivity values, firstly the VAR algorithm was applied to the data recorded over a sequence of 18 daily CH-ERT surveys (33,048 data). Then, the data belonging to five sets of measurements (9180 data) were used as "test data" for checking the predictive capabilities of the VAR algorithm.

In detail, the procedure for testing the VAR method is done as follows: First, the correlated historical data were used for creating a model of future trends of electric properties (such as apparent resistivity as well as resistances) over time, for each measurement point by applying Equations (4) and (5). Next, such predicted measurements were inverted for retrieving predicted resistivity models. The test data and models (effectively observed) were used for comparing predicted and true resistivity distributions.

Table 2 shows an example of a subset of experimental data (resistances measured at 10 quadrupoles) and the corresponding prediction for five future steps.

**Table 2.** Experimental measurements and corresponding predictions using Vector Autoregressive (VAR) statistical method.

| **Sequential ERT Surveys** | **Resistance at the Various Quadrupoles (Ω)** | | | | | | | | | |
|---|---|---|---|---|---|---|---|---|---|---|
| | Q1 | Q2 | Q3 | Q4 | Q5 | Q6 | Q7 | Q8 | Q9 | Q10 |
| STEP 10 | 1.76 | 19.16 | 8.80 | 1.65 | 12.03 | 14.33 | 16.15 | 13.40 | 19.71 | 8.88 |
| STEP 11 | 1.68 | 19.21 | 8.46 | 3.59 | 9.63 | 13.15 | 15.29 | 12.93 | 19.13 | 9.16 |
| STEP 12 | 1.74 | 19.13 | 8.46 | 3.09 | 10.06 | 13.33 | 15.60 | 13.20 | 19.66 | 9.37 |
| STEP 13 | 2.04 | 18.87 | 9.33 | 1.08 | 9.64 | 12.81 | 15.66 | 13.37 | 20.80 | 10.33 |
| STEP 14 | 1.66 | 19.07 | 8.47 | 3.17 | 10.78 | 13.17 | 15.32 | 12.75 | 19.46 | 9.25 |
| STEP 15 | 1.77 | 19.02 | 8.50 | 3.24 | 10-08 | 12.94 | 15.18 | 12.81 | 19.65 | 9.11 |
| STEP 16 | 1.92 | 18.90 | 8.40 | 2.95 | 10.79 | 13.19 | 15.29 | 12.66 | 19.42 | 9.39 |
| STEP 17 | 1.83 | 19.12 | 9.69 | 1.15 | 9.24 | 12.72 | 16.72 | 14.35 | 21.21 | 11.87 |
| STEP 18 | 1.84 | 18.29 | 7.29 | 0.22 | 11.95 | 16.95 | 15.46 | 15.47 | 19.09 | 12.43 |
| **Sequential Predictions** | **Predicted resistance at the Various Quadrupoles (Ω)** | | | | | | | | | |
| PRED 1 | 1.85 | 18.80 | 8.47 | 1.38 | 10.95 | 14.07 | 15.80 | 14.12 | 20.05 | 11.10 |
| PRED 2 | 1.86 | 18.77 | 8.47 | 1.25 | 11.04 | 14.12 | 15.84 | 14.19 | 20.09 | 11.24 |
| PRED 3 | 1.87 | 18.75 | 8.47 | 1.12 | 11.12 | 14.18 | 15.88 | 14.27 | 20.13 | 11.37 |
| PRED 4 | 1.88 | 18.72 | 8.47 | 0.99 | 11.21 | 14.24 | 15.92 | 14.35 | 20.17 | 11.50 |
| PRED 5 | 1.89 | 18.69 | 8.47 | 0.88 | 11.29 | 14.30 | 15.96 | 14.43 | 20.22 | 11.63 |

Electrical resistivity tomography (CH-ERT), prediction (PRED), quadrupole (Q).

Furthermore, RNN was tested to the same dataset. Like in the VAR method, the crucial step consists of creating a predictive model using historical data. In this case, a Recurrent Neural Network was used with an architecture similar to the one shown in Figure 2. As explained in the Section 2.2.2, a Long-Short Term Memory (LSTM) algorithm is used for retrieving a multivariate predictive function from various sequences of correlated historical data. For that purpose, different numbers of monitoring surveys were tested (ranging from 2 to 20, 1 per day), in order to compare various predictive models. Since the electrical measurements taken at adjacent electrodes are strongly correlated, it is possible to assume that a number between 10 and 20 monitor surveys should be sufficient for building an effective historical dataset for Recurrent Neural Network application.

In general, the performance of the prediction can be assessed by estimating the average forecast error on known data. What is done is to verify how far the forecast of the observations is wrong for known observations, assuming that they are not known to the predictive algorithm.

As an example, Figure 6 shows a chart of predictions (predicted future) vs. observations (true future) for a given quadrupole (Q1). The red and blue dots represent the normalized resistance values (ordinate axis) for a single measurement quadrupole, for various time steps (abscissa axis). In detail, 10 historical surveys were proved to be the right compromise between prediction reliability and number of surveys in test data. The Figure 6 shows that four out of five forecasts are excellent (error of about 1–2%). One of the values

(at the third time step in the "future") shows much less prediction accuracy (outlier?). The same graph is calculated for each quadrupole. For this dataset, the prediction uncertainties range between ±1% and ±5%.

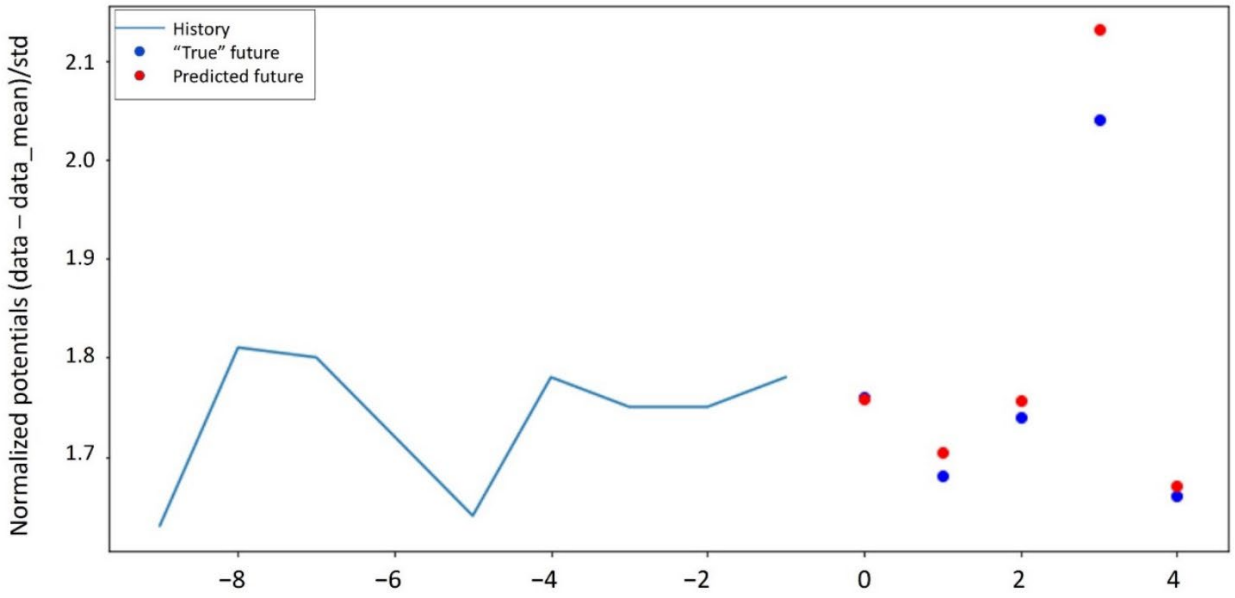


**Figure 6.** Chart of four predictions (predicted future) vs. observations ("true" future) for a single quadrupole (Q1—field data). Remark: time step "0" corresponds to the first prediction time step. The training dataset consists of 10 time steps.

In general, predictions retrieved by Recurrent Neural Network result are very consistent with the predictions shown in Table 2. The reason for this consistency probably arises in the fact that both the VAR and Neural Network methods are based on the same multivariate approach of data analysis. However, the principal advantage of RNN over VAR is that RNN can model a sequence of records so that each pattern can be assumed to be dependent on previous ones. In particular, LSTM allows for properly selecting the fraction of previous events to consider. This approach allows for properly managing complex historical datasets, improving the reliability of the predictive model(s) [67].

### *4.2. Application of RNN to Laboratory Dataset*

In this second example, prevision capabilities of RNN were tested to multi temporal CH-ERT laboratory dataset described in Section 3.2. In this case, the procedure for training and testing of the RNN is similar to the one described in the previous paragraph.

Figure 7a,b shows two examples of predictions at two correspondent measurements points (quadrupoles 1 and 3). The lowest panel (Figure 7c) shows an example of the Loss function trend over 40 epochs (iterations of the ML model) in the training and validation process.

In detail, the training loss is a metric used to assess how the machine-learning (ML) model fits the training data and it represents the error (normalized or expressed in %) of the model on the training set. The validation loss is a metric used to assess the performance of a machine-learning model on the validation set. This is a portion of the dataset used to validate the performance of the ML model.

The effectiveness of the training can be appreciated by looking at the continuous decrease of the Loos function and the correspondent good match between predicted and true future measurements at each quadrupole.

In this case, 13 historical surveys were proved to be the right compromise between prediction reliability and number of surveys in test data. The prediction uncertainties ranged between ±1% and ±3%.

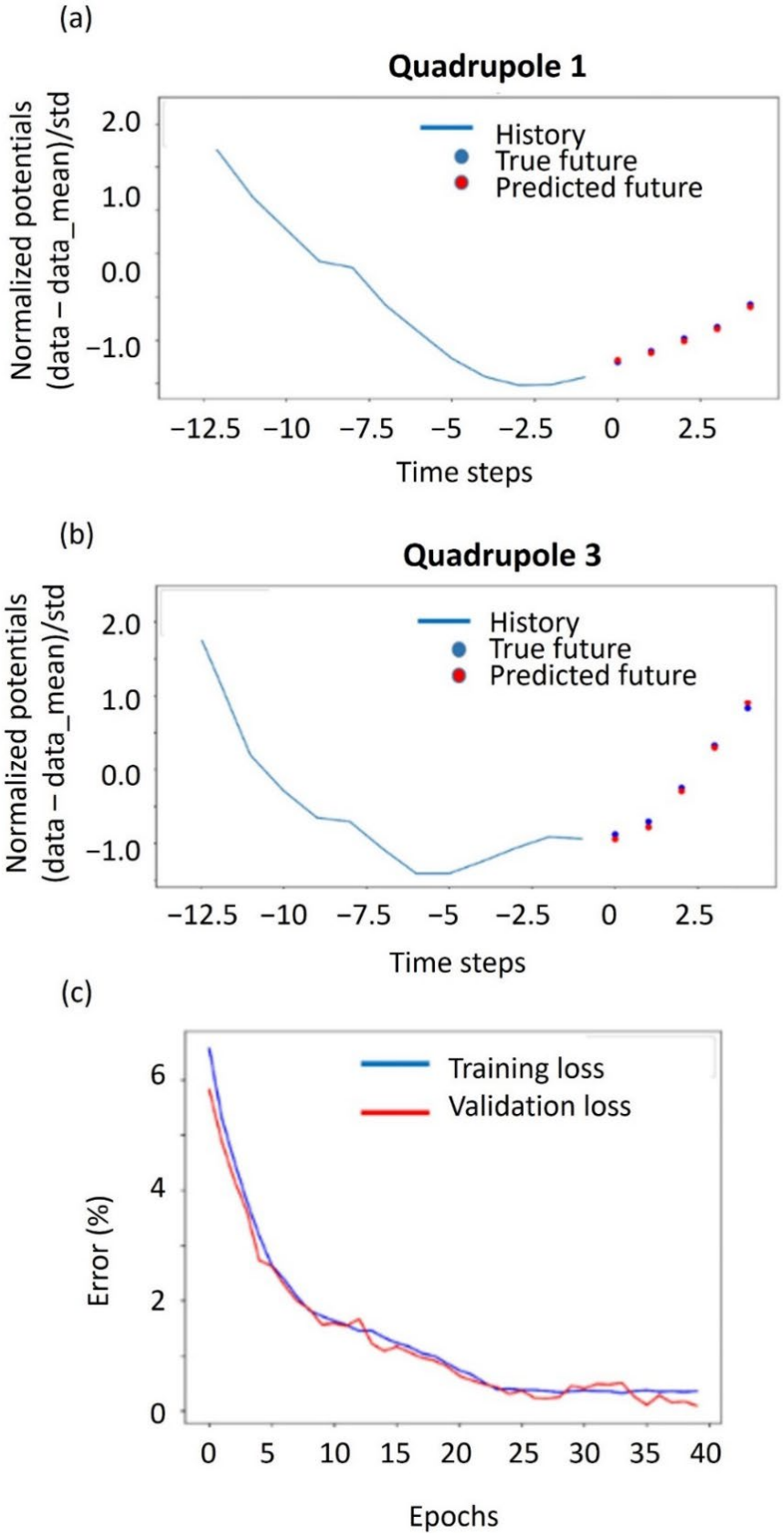


**Figure 7.** (**a**,**b**) Examples of RNN's predictions (normalized electrical potentials vs. time); (**c**) Loss function convergence trend (bottom-right panel). The training dataset consists of 13 time steps.

## 5. Discussion

Incorporation of two- and three-dimensional densely sampled geophysical data with conventional hydrological data increases the amount of data available for the hydrogeological system characterization, and thus has the potential to significantly improve the estimates of hydraulic properties and their spatial correlation over those estimates obtained from borehole data alone, as well as to provide this information at the relevant spatial scale [8,68]. Therefore, predicting the evolution of the geoelectrical response associated with fluids/contaminant displacements is extremely useful for defining an optimal aquifer management policy; modelling is indispensable to understand past and present conditions and for predicting and managing the future states of groundwater processes.

### 5.1. Field Experiment: Prediction of Saline Tracer Displacement

Acquired and "predicted" datasets were inverted with the open source ResIPy software package [62] and the "pyres" Python wrapper package, which allows for creating a flexible user interface for modelling and inversion of ERT datasets using the NumPy, SciPy, and Matplotlib Python packages [62,63]. In particular, the time-lapse inversion strategy used was difference inversion, after LaBrecque and Yang [69], because small changes of conductivity are better resolved, as in this experimental case, and high-quality images with fewer artefacts are produced.

In detail, the resistivity obtained by the inversion of background data (10 July) serves as the a priori model in the difference inversion. There are several advantages to this method. First, convergence is fast since the inverse routine needs only to find small perturbations about a good initial guess. Second, systematic errors, such as those due to errors in field configuration and discretization errors in the forward modelling algorithm, tend to be cancelled [69].

Then, CH-ERT imaging of tracer transport is best presented using images of resistivity change (%) relative to the pre-tracer condition according to the following:

$$d(\%) = \left[\frac{\rho_t - \rho_0}{\rho_0}\right] \times 100 \quad (9)$$

where 0% indicates no change between datasets, whereas negative values indicate an electrical resistivity decrease.

Images of electrical resistivity changes between −30 and −42 m (Figure 8) allow us to delineate salt plume evolution: they show evidence for a prevalent transport pathway under 30 m depth. Moreover, statistical predicted datasets seem to predict the tracer phenomenon well in the real aquifer studied here.

### 5.2. Laboratory Experiment: Prediction of Contamination Evolution

Predicted apparent electrical resistivity values were inverted using the open-source software ResIPy for retrieving correspondent predicted resistivity sections [62]. The area under investigation was discretized using a node-centered, 2D, triangular mesh and dividing the area into two regions: the outer one, characterized by fixed very high resistivity values to account for tank finite boundaries; and the inner region for the sand body, characterized by a starting resistivity of 100 Ωm.

Figure 9a shows the starting resistivity model before the salt solution injection. The measured resistivity values range between 1 and 50 Ωm. Higher values are probably associated to noisy electrodes. In Figure 9b, CH-ERT imaging following the solution injection are presented as resistivity change (%) relative to the pre-tracer condition (0% for no change between datasets, negative values for electrical resistivity decrease). Moreover, an example of a predicted resistivity model is shown retrieved from the previous "historical data" used for training the network.

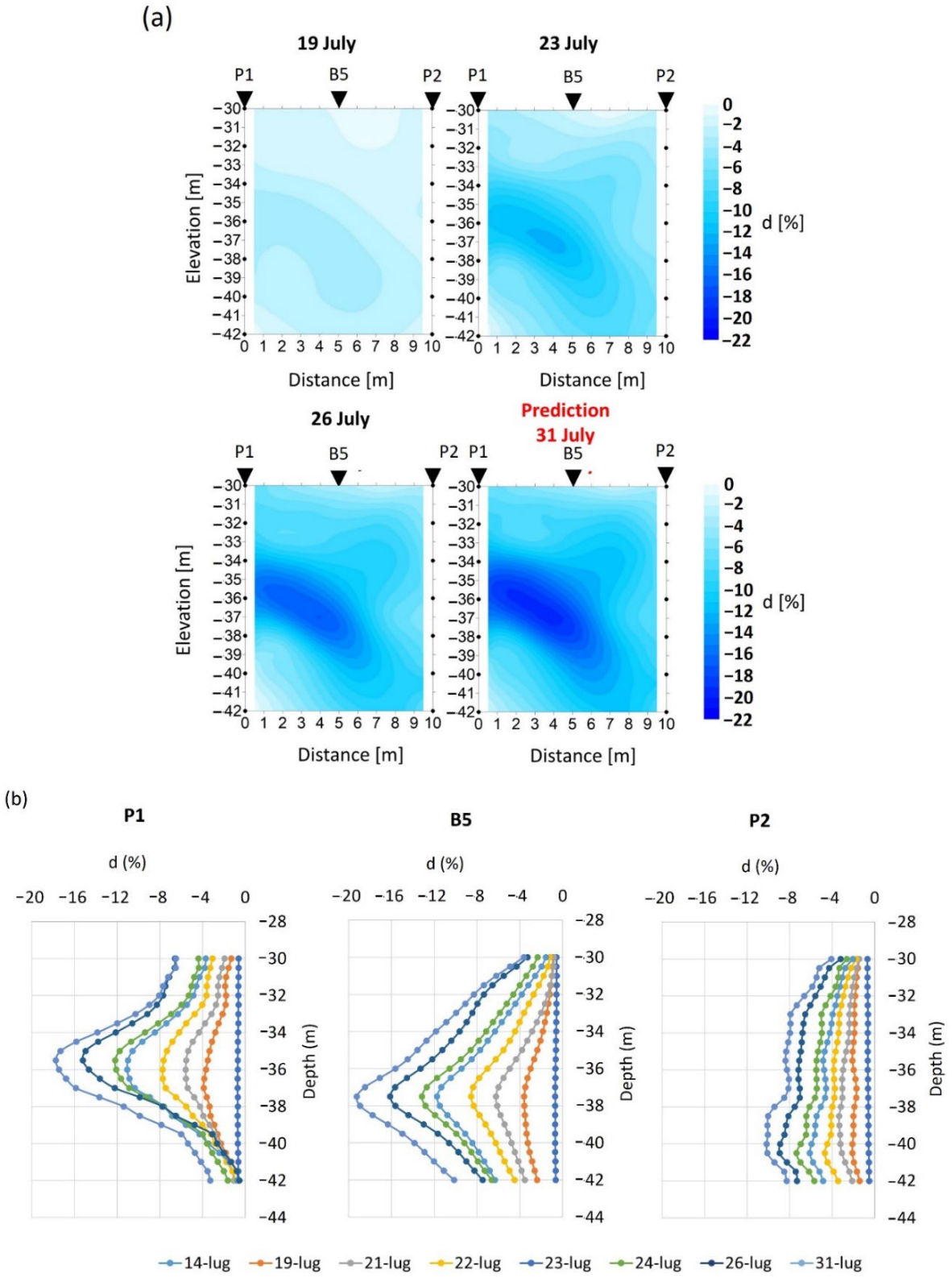


**Figure 8.** (**a**) Some images of resistivity variation (d, %) after tracer injection. Black dots are electrodes, and P1, P2, and B5 are piezometers; (**b**) electrical resistivity variation (d, %) curves along the piezometers P1, B5, and P2 from the CH-ERT dataset. Values at days 29 and 31 were estimated from CH-ERT predicted datasets.

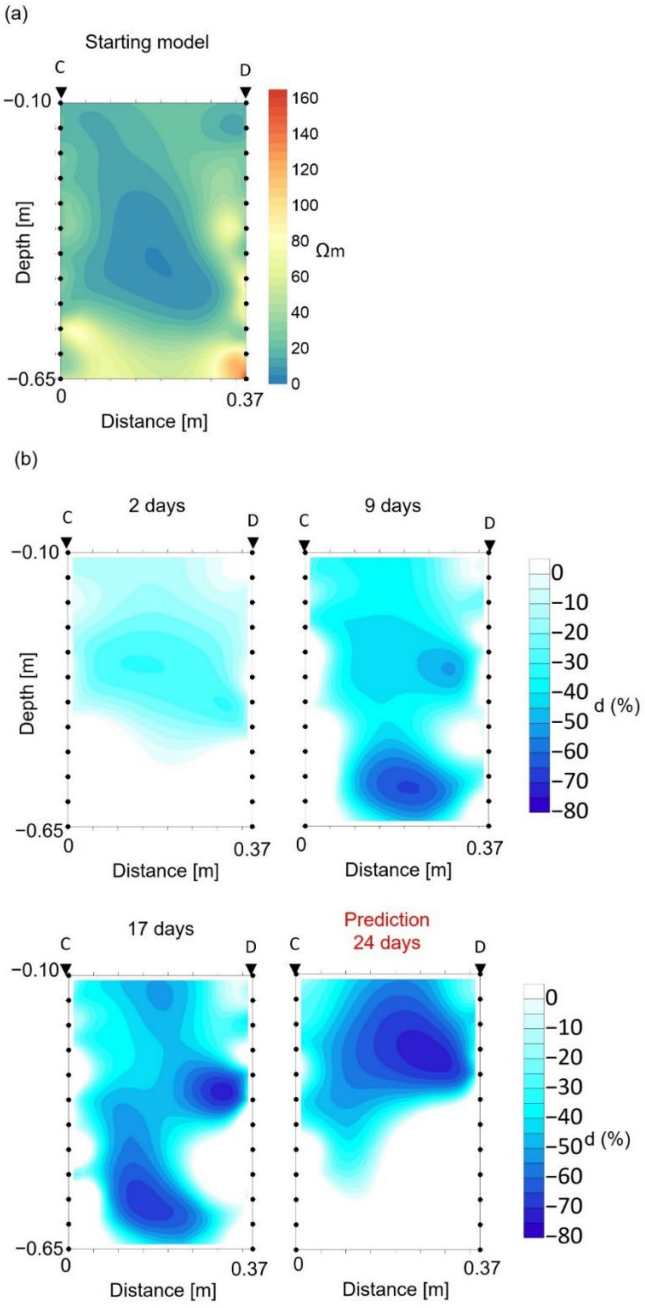


**Figure 9.** (**a**) True resistivity model obtained using ResIPy software of pre contamination condition; (**b**) images of resistivity variation (d, %) after salt solution injection. Black dots are electrodes, C and D are piezometers.

Electrical resistivity method is an effective tool to determine the Total Dissolved Solids (TDS) concentration if electrical resistivity of the formation and porosity are known. The possibility to correlate TDS with electrical resistivity is showed by Archie [70], who proposed an empirical relationship between formation electrical resistivity ($\rho_b$, Ωm) and pore water electrical resistivity ($\rho_w$, Ωm) according to the following equation:

$$\rho_b = a\varphi^{-m}S^{-n}\rho_w \quad (10)$$

where $a$ is the pore geometry coefficient (usually $a = 1$), $\varphi$ is the porosity, $m$ is the cementation factor (dimensionless, $1.14 \leq m \leq 2.9$ [71]), $S$ is the saturation degree, and $n$ is the saturation exponent [72].

In fully saturated conditions ($S$ = 1), this equation can be rearranging introducing the formation factor $F$ defined as:

$$F = \frac{a}{\varphi^m} = \frac{\rho_b}{\rho_w}. \quad (11)$$

Assuming for the simulated sandy aquifer a constant value for $F$ (homogenous sand), it is possible to define the saturation degree as:

$$S^{-n} = \frac{\rho_b}{\rho_w F}. \quad (12)$$

The electrical conductivity of groundwater (normalized to 25 °C) is directly related to the *TDS* based on the assumption that *TDS* in the water consist mainly of ionic constituents that conduct electricity [73]. In detail, the correlation of *TDS* and solution electrical conductivity ($\sigma$ in S/m = $1/\rho$) at the specified temperature T = 25 °C can be estimated by the following equation:

$$TDS = k_e \sigma \quad (13)$$

where $k_e$ will increase along with the increase of ions in water *TDS* is expressed in g/L and $\sigma$ in mS/cm. Therefore, considering $k_e$ = 0.7 (saline water with $\sigma$ from 1 till 45 mS/cm [74]), *TDS* (g/L) in the saturated zone can be obtained with the relation:

$$TDS = 7\frac{FS^{-n}}{\rho_b}. \quad (14)$$

For the studied case, $\rho_b$ (Ωm) was obtained by CH-ERT monitoring, porosity was 0.45, $m$ = 1.14, and $n$ =1.5 [64,65], while saturation degree in the vadose zone was estimated by numerical models [66].

Figure 10 shows the 3D representation of *TDS* > 10 g/L allowing us to delineate the salt plume evolution under 30 cm depth at 10, 18, and 24 days after the NaCl solution injection. *TDS* values at day 24 were estimated from CH-ERT predicted datasets.

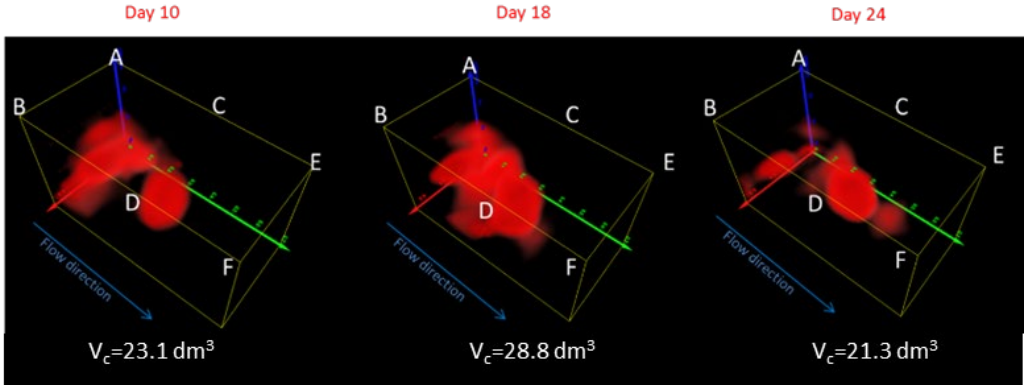


**Figure 10.** In red is the 3D distribution of *TDS* > 10 g/L obtained from predicted CH-ERT. A–F are piezometers, $V_c$ is the contaminated volume. *TDS* values at day 24 were estimated from CH-ERT predicted datasets. The 3D distribution was obtained with Paraview software (version 5.6.0, Kitware, Sandia National Labs, Los Alamos nat. lab., ASC and ARL, https://www.paraview.org/, accessed on 13 June 2022).

## 6. Summary of Results

In detail, the following are the most relevant results of the proposed approach:

- In the field experiment, based on multiple monitor geoelectrical surveys in cross-hole configuration, multiple resistivity models changing over a period of 28 days of the tracer test were defined;
- A variational statistical method was applied for predicting electrical resistivity variations;

- Transport characteristics of the studied aquifer were evaluated through both measured and predicted electrical resistivity data;
- This predictive approach can be applied for defining optimal aquifer management policy;
- In the lab experiment, Recurrent Neural Networks to retrieve a Multivariate LSTM Forecast Dynamic Model of the tracer displacements over time were applied;
- The predictions obtained through RNN are fully consistent with the evolution of the experimental system effectively observed, confirming the effectiveness of such a type of approach applied to predictive analysis of hydrogeological time-series;
- The predictions are based on the history path of electric potentials recorded through multiple surveys including thousands of measurement points.

## 7. Conclusions

Different statistical and machine-learning algorithms are commonly applied in various fields (such as in financial studies as well as in climatology, and so forth) to predict the future behavior of complex dynamic systems. However, no works are reported in the literature on their use for multi temporal geophysical data forecasting in near-surface applications.

In this work, both variational methods (VAR) and machine-learning algorithms (Recurrent Neural Networks) were tested for predicting the values of cross-hole electrical resistivity data, taking in account measurements recorded during a tracer test monitoring experiments performed, respectively, during a previous work on a heterogeneous aquifer in the south of Italy [55] and in a new controlled laboratory experiment. The aim was to predict the geoelectrical variations induced by fluids/contaminant displacements in the subsoil.

This study shows that VAR and RNN can be effective tools for predicting the values of cross-hole geoelectrical data for subsoil fluid transport monitoring in a relatively simple hydrogeological context where seasonal changes in temperature, subsoil saturation degree, and groundwater level variation are negligible. In particular, RNN showed a very good performance even with a small historical dataset.

However, starting from a bigger historical dataset, and by entering more control factors and increasing the variables of subsurface response, it will be possible to extend the forecast to more than five previsions. In this manner, an efficient quantification of transport characteristics at a study site could follow from the integration of direct hydrological data, and a relatively "small" number of geoelectrical measurements and probabilistic previsions based on electrical images.

Finally, we remark that the proposed methodology is potentially applicable also in the energetic sector for the reservoirs management during oil, gas, hydrogen, $CO_2$, and heat storage or extraction.

**Author Contributions:** Conceptualization, V.G., P.D. and E.R.; Data curation, V.G. and L.C.; Formal analysis, P.D.; Funding acquisition, E.R.; Investigation, V.G., L.C., G.D.M. and E.R.; Methodology, V.G., P.D., L.C., G.D.M. and E.R.; Project administration, E.R.; Software V.G., P.D. and L.C.; Supervision, E.R.; Validation, V.G., P.D. and E.R.; Visualization, V.G., P.D., L.C. and E.R.; Writing—original draft, V.G. and P.D.; Writing—review and editing, V.G., P.D., L.C. and E.R. All authors have read and agreed to the published version of the manuscript.

**Funding:** Laboratory experiment was funded by the Basilicata Region, Progetto PO FSE Basilicata 2007–2013: "Promozione della ricerca e dell'innovazione e sviluppo di relazioni con il sistema produttivo regionale" DD n. 796/2013 Azione n. n. 15/AP/05/2013/REG.

**Institutional Review Board Statement:** Not applicable.

**Informed Consent Statement:** Not applicable.

**Data Availability Statement:** The data that support the findings of this study are available from the corresponding author upon request. Python codes are available from Paolo Dell'Aversana upon request.

**Acknowledgments:** The filed experimental work was provided in collaboration with Salvatore Straface and Francesco Chidichimo of University of Calabria. Authors are grateful to the Director of the CNR-IMAA for the experimental phase in the Laboratory Hydrogeosite facility. Authors thank Rosy Colaiacovo and Serena Parisi for their support during the laboratory experiment.

**Conflicts of Interest:** The authors declare no conflict of interest.

## References

1. Amanambu, A.C.; Obarein, O.A.; Mossa, J.; Li, L.; Ayeni, S.S.; Balogun, O.; Oyebamiji, A.; Ochege, F.U. Groundwater system and climate change: Present status and future considerations. *J. Hydrol.* **2020**, *589*, 125163. [CrossRef]
2. Lall, U.; Josset, L.; Russo, T. A Snapshot of the World's Groundwater Challenges. *Annu. Rev. Environ. Resour.* **2020**, *45*, 171–194. [CrossRef]
3. Wu, W.Y.; Lo, M.H.; Wada, Y.; Famiglietti, J.S.; Reager, J.T.; Yeh, P.J.-F.; Ducharne, A.; Yang, Z.-L. Divergent effects of climate change on future groundwater availability in key mid-latitude aquifers. *Nat. Commun.* **2020**, *11*, 3710. [CrossRef] [PubMed]
4. Nordin, N.F.C.; Mohd, N.S.; Koting, S.; Ismail, Z.; Sherif, M.; El-Shafie, A. Groundwater quality forecasting modelling using artificial intelligence: A review. *Groundw. Sustain. Dev.* **2021**, *14*, 100643. [CrossRef]
5. Zehe, E.; Loritz, R.; Edery, Y.; Berkowitz, B. Preferential pathways for fluid and solutes in heterogeneous groundwater systems: Self-organization, entropy, work. *Hydrol. Earth Syst. Sci.* **2021**, *25*, 5337–5353. [CrossRef]
6. Zhang, X.; Ma, F.; Yin, S.; Wallace, C.D.; Soltanian, M.R.; Dai, Z.; Ritzi, R.W.; Ma, Z.; Zhan, C.; Lü, X. Application of upscaling methods for fluid flow and mass transport in multi-scale heterogeneous media: A critical review. *Appl. Energy* **2021**, *303*, 117603. [CrossRef]
7. Tao, H.; Hameed, M.M.; Marhoon, H.A.; Zounemat-Kermani, M.; Heddam, S.; Kim, S.; Sulaiman, S.O.; Tan, M.L.; Sa'adi, Z.; Mehr, A.D.; et al. Groundwater level prediction using machine learning models: A comprehensive review. *Neurocomputing* **2022**, *489*, 271–308. [CrossRef]
8. Hubbard, S.S.; Rubin, Y. Hydrogeological parameter estimation using geophysical data: A review of selected techniques. *J. Contam. Hydrol.* **2000**, *45*, 3–34. [CrossRef]
9. Sandberg, S.K.; Slater, L.D.; Versteeg, R. An integrated geophysical investigation of the hydrogeology of an anisotropic unconfined aquifer. *J. Hydrol.* **2022**, *267*, 227–243. [CrossRef]
10. Doetsch, J.; Linde, N.; Vogt, T.; Binley, A.; Green, A.G. Imaging and quantifying salt-tracer transport in a riparian groundwater system by means of 3D ERT monitoring. *Geophysics* **2012**, *77*, B207–B218. [CrossRef]
11. Fernández de Vera, N.; Beaujean, J.; Jamin, P.; Hakoun, V.; Caterina, D.; Dahan, O.; Vanclooster, M.; Dassargues, A.; Nyugen, F.; Brouyère, S. Tracer experiment in a brownfield using geophysics and a vadose zone monitoring system. *Vadose Zone J.* **2017**, *16*, 1–15. [CrossRef]
12. McLachlan, P.J.; Chambers, J.E.; Uhlemann, S.S.; Binley, A. Geophysical characterisation of the groundwater–surface water interface. *Adv. Water Resour.* **2017**, *109*, 302–319. [CrossRef]
13. Bouzaglou, V.; Crestani, E.; Salandin, P.; Gloaguen, E.; Camporese, M. Ensemble Kalman Filter Assimilation of ERT Data for Numerical Modeling of Seawater Intrusion in a Laboratory Experiment. *Water* **2018**, *10*, 397. [CrossRef]
14. Binley, A. 11.08-Tools and Techniques: Electrical Methods. In *Treatise on Geophysics*; Schubert, G., Ed.; Elsevier: Amsterdam, The Netherlands, 2015; pp. 233–259.
15. Glover, P.W.J. 11.0-Geophysical Properties of the Near Surface Earth: Electrical Properties. In *Treatise on Geophysics*; Schubert, G., Ed.; Elsevier: Amsterdam, The Netherlands, 2015; pp. 89–137.
16. Binley, A.; Cassiani, G.; Middleton, R.; Winship, P. Vadose zone flow model parameterisation using cross-borehole radar and resistivity imaging. *J. Hydrol.* **2002**, *267*, 147–159. [CrossRef]
17. Perri, M.T.; Cassiani, G.; Gervasio, I.; Deiana, R.; Binley, A. A saline tracer test monitored via both surface and cross-borehole electrical resistivity tomography: Comparison of time-lapse results. *J. Appl. Geophys.* **2012**, *79*, 6–16. [CrossRef]
18. Karaoulis, M.; Tsourlos, P.; Kim, J.H.; Revil, A. 4D time-lapse ERT inversion: Introducing combined time and space constraints. *Near Surf. Geophys.* **2014**, *12*, 25–34. [CrossRef]
19. Watlet, A.; Kaufmann, O.; Triantafyllou, A.; Poulain, A.; Chambers, J.E.; Meldrum, P.I.; Wilkinson, P.B.; Hallet, V.; Quinif, Y.; Van Ruymbeke, M.; et al. Imaging groundwater infiltration dynamics in the karst vadose zone with long-term ert monitoring. *Hydrol. Earth Syst. Sci.* **2018**, *22*, 1563–1592. [CrossRef]
20. Mary, B.; Peruzzo, L.; Boaga, J.; Cenni, N.; Schmutz, M.; Wu, Y.; Hubbard, S.S.; Cassiani, G. Time-lapse monitoring of root water uptake using electrical resistivity tomography and mise-à-la-masse: A vineyard infiltration experiment. *Soil* **2020**, *6*, 95–114. [CrossRef]
21. Lapenna, V.; Perrone, A. Time-Lapse Electrical Resistivity Tomography (TL-ERT) for Landslide Monitoring: Recent Advances and Future Directions. *Appl. Sci.* **2022**, *12*, 1425. [CrossRef]
22. Folch, A.; del Val, L.; Luquot, L.; Martínez-Pérez, L.; Bellmunt, F.; Le Lay, H.; Rodellas, V.; Ferrer, N.; Palacios, A.; Fernández, S.; et al. Combining fiber optic DTS, cross-hole ERT and time-lapse induction logging to characterize and monitor a coastal aquifer. *J. Hydrol.* **2020**, *588*, 125050. [CrossRef]

23. Palacios, A.; Ledo, J.J.; Linde, N.; Luquot, L.; Bellmunt, F.; Folch, A.; Marcuello, A.; Queralt, P.; Pezard, P.A.; Martínez, L.; et al. Time-lapse cross-hole electrical resistivity tomography (CHERT) for monitoring seawater intrusion dynamics in a Mediterranean aquifer. *Hydrol. Earth Syst. Sci.* **2020**, *24*, 2121–2139. [CrossRef]
24. Blazevic, L.A.; Bodet, L.; Pasquet, S.; Linde, N.; Jougnot, D.; Longuevergne, L. Time-Lapse Seismic and Electrical Monitoring of the Vadose Zone during a Controlled Infiltration Experiment at the Ploemeur Hydrological Observatory, France. *Water* **2020**, *12*, 1230. [CrossRef]
25. Almpanis, A.; Gerhard, J.; Power, C. Mapping and monitoring of DNAPL source zones with combined direct current resistivity and induced polarization: A field-scale numerical investigation. *Water Resour. Res.* **2021**, *57*, e2021WR031366. [CrossRef]
26. Nazifi, H.M.; Gülen, L.; Gürbüz, E.; Pekşen, E. Time-lapse electrical resistivity tomography (ERT) monitoring of used engine oil contamination in laboratory setting. *J. Appl. Geophys.* **2022**, *197*, 104531. [CrossRef]
27. Cannavò, F.; Cannata, A.; Donner, R.V.; Kanevski, M. Editorial: Advanced Time Series Analysis in Geosciences. *Front. Earth Sci.* **2022**, *9*, 666148. [CrossRef]
28. Hill, P.; Biggs, J.; Ponce-López, V.; Bull, D. Time-series prediction approaches to forecasting deformation in Sentinel-1 InSAR data. *J. Geophys. Res. Solid Earth* **2021**, *126*, e2020JB020176. [CrossRef]
29. Hewamalage, H.; Bergmeir, C.; Bandara, K. Recurrent Neural Networks for Time Series Forecasting: Current Status and Future Directions. *Int. J. Forecast.* **2020**, *37*, 388–427. [CrossRef]
30. Guzman, S.M.; Paz, J.O.; Tagert, M.L.M.; Mercer, A. Artificial neural networks and support vector machines: Contrast study for groundwater level prediction. In Proceedings of the ASABE Annual International Meeting, New Orleans, LA, USA, 26–29 July 2015; p. 1.
31. Valadkhan, D.; Moghaddasi, R.; Mohammadinejad, A. Groundwater quality prediction based on LSTM RNN: An Iranian experience. *Int. J. Environ. Sci. Technol.* **2022**, 12. [CrossRef]
32. Papacharalampous, G.; Tyralis, H.; Koutsoyiannis, D. One-step ahead forecasting of geophysical processes within a purely statistical framework. *Geosci. Lett.* **2018**, *5*, 12. [CrossRef]
33. Bhardwaj, S.; Chandrasekhar, E.; Padiyar, P.; Gadre, V.M. A comparative study of wavelet-based ANN and classical techniques for geophysical time-series forecasting. *Comput. Geosci.* **2020**, *138*, 104461. [CrossRef]
34. Dell'Aversana, P. Reinforcement Learning in Optimization Problems. Applications to Geophysical Data Inversion. *AIMS Geosci.* **2022**, *8*, 488–502. [CrossRef]
35. Dell'Aversana, P. Reservoir prescriptive management combining electric resistivity tomography and machine learning. *AIMS Geosci.* **2021**, *7*, 138–161. [CrossRef]
36. Lee, S.-J.; Yoon, H.-K. Discontinuity Predictions of Porosity and Hydraulic Conductivity Based on Electrical Resistivity in Slopes through Deep Learning Algorithms. *Sensors* **2021**, *21*, 1412. [CrossRef] [PubMed]
37. Dell'Aversana, P. Combining Geophysical Inversion with Reinforcement Learning. In Proceedings of the 83rd EAGE Annual Conference & Exhibition, Madrid, Spain, 6–9 June 2022; Volume 2022, pp. 1–5. [CrossRef]
38. Alali, A.; Kazei, V.; Sun, B.; Alkhalifah, T. Time-lapse data matching using a recurrent neural network approach. *Geophysics* **2022**, *87*, V405–V417. [CrossRef]
39. Kunetz, G. *Principles of Direct Current Resistivity Prospecting (Geoexploration Monographs, Series 1, Number 1)*; Schweizerbart Science Publishers: Stuttgart, Germany, 1966; 103p.
40. Shima, H. 2D and 3D resistivity image reconstruction using crosshole data. *Geophysics* **1992**, *57*, 1270–1281. [CrossRef]
41. Zhou, B.; Greenhalgh, S.A. A synthetic study on cross-hole resistivity imaging with different electrode arrays. *Explor. Geophys.* **1997**, *28*, 1–5.
42. *Exponential Smoothing for Predicting Demand*; Arthur, D. (Ed.) Little Inc.: Cambridge, MA, USA, 1956; p. 15.
43. Anderson, T.W. *An Introduction to Multivariate Statistical Analysis*; Wiley: New York, NY, USA, 1958; pp. 1–713.
44. Feinstein, A.R. *Multivariable Analysis: An Introduction*; Yale University Press: New Haven, CT, USA, 1996; pp. 1–613.
45. Johnson, R.A.; Wichern, D.W. *Applied Multivariate Statistical Analysis*, 6th ed.; Person New International Edition: London, UK, 2014; pp. 1–776.
46. Lütkepohl, H. *New Introduction to Multiple Time Series Analysis*; Springer: Berlin, Germany, 2005; pp. 1–553.
47. Asteriou, D.; Hall, S.G. Vector Autoregressive (VAR) Models and Causality Tests. In *Applied Econometrics*; Palgrave MacMillan: London, UK, 2011; pp. 319–333.
48. Barkan, O.; Benchimol, J.; Caspi, I.; Cohen, E.; Hammer, A.; Koenigstein, N. Forecasting CPI inflation components with Hierarchical Recurrent Neural Networks. *Int. J. Forecast.* **2022**, in press. [CrossRef]
49. Haşim, S.; Senior, A.; Beaufays, F. Long Short-Term Memory Recurrent Neural Network Architectures for Large Scale Acoustic Modelling. In Proceedings of the 15th Annual Conference of the International Speech Communication Association (INTERSPEECH 2014), Singapore, 14–18 September 2014.
50. Malhotra, P.; Vig, L.; Shroff, G.; Agarwal, P. Long Short Term Memory Networks for Anomaly Detection in Time Series. In Proceedings of the European Symposium on Artificial Neural Networks, Computational Intelligence and Machine Learning (ESANN 2015), Bruges, Belgium, 22–24 April 2015.
51. Sherstinsky, A. Fundamentals of Recurrent Neural Network (RNN) and Long Short-Term Memory (LSTM) Network. *Physica D* **2020**, *404*, 132306. [CrossRef]

52. Saad, E.W.; Prokhorov, D.V.; Wunsch, D.C. Comparative study of stock trend prediction using time delay, recurrent and probabilistic neural networks. *IEEE Trans. Neural Netw.* **1998**, *9*, 1456–1470. [CrossRef]
53. Tealab, A.; Hefny, H.; Badr, A. Forecasting of nonlinear time series using ANN. *Future Comput. Inform. J.* **2017**, *2*, 39–47. [CrossRef]
54. Sagheer, A.; Kotb, M. Time series forecasting of petroleum production using deep LSTM recurrent networks. *Neurocomputing* **2019**, *323*, 203–213. [CrossRef]
55. Giampaolo, V.; Rizzo, E.; Straface, S.; Votta, M. Hydrogeophysics techniques for the characterization of a heterogeneous aquifer. *Boll. Di Geofis. Teor. Ed Appl.* **2011**, *52*, 595–606.
56. Giampaolo, V.; Rizzo, E.; Straface, S.; Chidichimo, F.; Votta, M. Hydrogeophysical methods for saline tracer test. In Proceedings of the 1st International Workshop: Methods and Technologies for Environmental Monitoring and Modelling: Landslides and Groundwater Dynamics, Potenza, Italy, 29 September–3 October 2011; pp. 159–162.
57. Giampaolo, V.; Rizzo, E.; Straface, S.; Chidichimo, F.; Votta, M. Transport processes in porous media by geophysical methods. In Proceedings of the XXX Convegno Nazionale del Gruppo Nazionale di Geofisica della Terra Solida (GNGTS), Trieste, Italy, 14–17 November 2011; pp. 568–571.
58. Giampaolo, V. Hydrogeophysical Methods for Soils and Groundwater Contamination. Ph.D. Thesis, The Basilicata University, Potenza, Italy, 2013.
59. Troisi, S.; Fallico, C.; Straface, S.; Migliari, E. Application of kriging with external drift to estimate hydraulic conductivity from electrical resistivity data in unconsolidated deposits near Montalto Uffugo, Italy. *Hydrogeol. J.* **2000**, *8*, 356–367. [CrossRef]
60. Rizzo, E.; Suski, B.; Revil, A.; Straface, S.; Troisi, S. Self-potential signals associated with pumping-tests experiments. *J. Geophys. Res.* **2004**, *109*, B10203. [CrossRef]
61. Straface, S.; Fallico, C.; Troisi, S.; Rizzo, E.; Revil, A. An inverse procedure to estimate transmissivity from heads and SP signals. *Ground Water* **2007**, *45*, 420–428. [CrossRef]
62. Blanchy, G.; Saneiyan, S.; Boyd, J.; McLachlan, P.; Binley, A. ResIPy, an intuitive open source software for complex geoelectrical inversion/modelling. *Comput. Geosci.* **2020**, *137*, 104423. [CrossRef]
63. Befus, K.M. Pyres: A Python Wrapper for Electrical Resistivity Modeling with R2. *J. Geophys. Eng.* **2018**, *15*, 338–346. [CrossRef]
64. Capozzoli, L.; De Martino, G.; Giampaolo, V.; Parisi, S.; Rizzo, E. Integrated geophysical and hydraulic methodologies for the study of contaminant transport process in the subsoil: A sand box experiment. In Proceedings of the XXXIII Convegno Nazionale del Gruppo Nazionale di Geofisica della Terra Solida (GNGTS), Bologna, Italy, 25–27 November 2014; pp. 143–149.
65. Capozzoli, L. Electric and Electromagnetic Geophysical Methods for the Characterization and Monitoring of Contamination Phenomena in the Subsoil. Ph.D. Thesis, The Basilicata University, Potenza, Italy, 2014.
66. Straface, S.; Rizzo, E.; Chidichimo, F. Estimation of hydraulic conductivity and water table map in a large-scale laboratory model by means of the self-potential method. *J. Geophys. Res.* **2011**, *115*, B06105. [CrossRef]
67. Van Houdt, G.; Mosquera, C.; Nápoles, G. A review on the long short-term memory model. *Artif. Intell. Rev.* **2020**, *53*, 5929–5955. [CrossRef]
68. Christensen, N.K.; Christensen, S.; Ferre, T.P.A. Testing alternative uses of electromagnetic data to reduce the prediction error of groundwater models. *Hydrol. Earth Syst. Sci.* **2016**, *20*, 1925–1946. [CrossRef]
69. LaBrecque, D.J.; Yang, X. Difference inversion of ERT data. A fast inversion method for 3-D in situ monitoring. *J. Environ. Eng. Geophys.* **2001**, *6*, 83–89. [CrossRef]
70. Archie, G.E. The Electrical Resistivity Log as an Aid in Determining Some Reservoir Characteristics. *Trans. AIME* **1942**, *146*, 54–62. [CrossRef]
71. Schön, J.H. *Physical Properties of Rocks: Fundamentals and Principles of Petrophysics*; Elsevier: Amsterdam, The Netherlands, 2004; pp. 1–600.
72. Riedel, M.; Collett, T.S.; Hyndman, R.D. *Gas Hydrate Concentration Estimates from Chlorinity, Electrical Resistivity, and Seismic Velocity*; Open-File Rep. 4934; Geological Survey of Canada: Ottawa, ON, Canada, 2005.
73. Atekwanaa, E.A.; Atekwanaa, E.; Roweb, R.S.; Werkema, D.D.; Legalld, F.D. The relationship of total dissolved solids measurements to bulk electrical conductivity in an aquifer contaminated with hydrocarbon. *J. Appl. Geophys.* **2004**, *56*, 281–294. [CrossRef]
74. Rusydi, A.F. Correlation between conductivity and total dissolved solid in various type of water: A review. *IOP Conf. Ser. Earth Environ. Sci.* **2018**, *118*, 012019. [CrossRef]